Monthly Notices of the ROYAL ASTRONOMICAL SOCIETY

MNRAS **530,** 2273–2281 (2024) https://doi.org/10.1093/mnras/stae952
Advance Access publication 2024 April 18

Apparent correlation between extrinsic and intrinsic flux variations in the first gravitationally lensed quasar

L. J. Goicoechea,[1,2]★ V. N. Shalyapin[2,3]★ and A. Oscoz[4,5]★

[1]*Instituto de Física de Cantabria (CSIC-UC), Avda. de Los Castros s/n, E-39005 Santander, Spain*
[2]*Departamento de Física Moderna, Universidad de Cantabria, Avda. de Los Castros s/n, E-39005 Santander, Spain*
[3]*O.Ya. Usikov Institute for Radiophysics and Electronics, National Academy of Sciences of Ukraine, 12 Acad. Proskury St., UA-61085 Kharkiv, Ukraine*
[4]*Instituto de Astrofísica de Canarias (IAC), c/ Vía Láctea s/n, E-38205 La Laguna, Spain*
[5]*Departamento de Astrofísica, Universidad de La Laguna, E-38200 La Laguna, Spain*

Accepted 2024 April 3. Received 2024 April 2; in original form 2023 October 28

ABSTRACT

To better understand which sources contribute to optical passband fluxes of Q0957+561, we present and analyse light curves of the doubly imaged gravitationally lensed quasar from its discovery to 2023. After an early microlensing event, the difference light curves (describing delay-corrected flux ratios between the two quasar images) only show prominent microlensing gradients over the last 17 yr. In addition to these long time-scale gradients in the *gr* bands, we detect short time-scale, extrinsically induced differential variations that are highly correlated with the short time-scale intrinsic variability of the quasar in those bands. Both the accretion disc and the broad emission-line region (BELR) contribute to optical passband fluxes, and we also show that realistic contributions of the BELR account for the observed correlations in the *gr* bands. We would like to highlight that the BELR sources of optical passband fluxes of Q0957+561 should be taken into account when measuring accretion-disc source sizes from microlensing simulations.

Key words: accretion, accretion discs – gravitational lensing: micro – gravitational lensing: strong – quasars: individual: Q0957+561.

1 INTRODUCTION

The first gravitational lens system was discovered 44 yr ago (Walsh, Carswell & Weymann 1979). The gravitational field of a galaxy cluster at redshift $z = 0.36$ produces two images, A and B, of the background quasar Q0957+561 at redshift $z = 1.41$ (Stockton 1980; Young et al. 1980; Garrett, Walsh & Carswell 1992). Although the entire gravitational lens is a galaxy cluster, the main deflector is a giant elliptical galaxy close to the image B. Optical passband fluxes are mainly due to nuclear continuum emission, and analysing the optical passband variability of both quasar images, it has also been established that intrinsic flux variations in B lag those in A by $\Delta t \sim 14$ months (e.g. Vanderriest et al. 1989; Kundić et al. 1997; Oscoz et al. 1997, 2001; Shalyapin et al. 2008). After accounting for this time delay, the optical-passband flux ratio $F_{\rm opt} = F_{\rm B}(t)/F_{\rm A}(t - \Delta t)$ is related to the lens magnification ratio and the intervening medium along the lines of sight towards the two quasar images. The lens magnification ratio is an achromatic and stationary factor, while dust clouds and compact objects (e.g. stars) within the main lens galaxy at $z = 0.36$ may produce chromaticity and/or variability in $F_{\rm opt}$ (e.g. Chang & Refsdal 1979; Nadeau et al. 1991).

Radio core fluxes of Q0957+561 come from a large source, so they are not affected by gravitational microlensing by compact objects. In addition, dust extinction does not play a role at radio wavelengths. Thus, the radio-core flux ratio $F_{\rm radio} = 0.75 \pm 0.02$ (Conner, Lehar & Burke 1992; Garrett et al. 1994) is a good proxy of the lens magnification ratio. Moreover, based on accurate delay-corrected flux ratios, there is also strong evidence that the C III] and Mg II broad-line emissions are practically unaffected by extinction and microlensing (Schild & Smith 1991; Goicoechea, Gil-Merino & Ullán 2005; Gil-Merino et al. 2018). Using *Hubble Space Telescope* (*HST*) spectra of Q0957+561 in a quiescent phase of microlensing activity (UV–optical data in the years 1999 and 2000, see below), Goicoechea et al. (2005) reported on the chromatic behaviour of $F_{\rm UV\text{-}opt}$, which resembles extinction laws for galaxies in the Local Group. They found $F_{\rm UV\text{-}opt} > 1$ at all UV–optical continuum wavelengths, indicating that the A image is more affected by dust. The simplest scenario consists of a dust cloud in front of the image A. This cloud must be small enough not to produce extinction over the broad emission-line region (BELR) as a whole.

Very rapid fluctuations in the optical-passband flux ratio of Q0957+561 are most likely due to observational noise (e.g. Gil-Merino et al. 2001), while longer time-scale fluctuations are thought to be caused by gravitational microlensing. The B image passes through an inner, very dense region of the giant elliptical galaxy, and Refsdal et al. (2000) considered microlensing effects on this image

★ E-mail: goicol@unican.es (LJG); vshal@ukr.net (VNS); alex.oscoz@iac.es (AO)

to interpret a fluctuation in the *R* band in the 1980s lasting 5 yr. After the early years event, $F_{\rm opt}$ in red passbands did not show prominent events/gradients over about 20 yr, and then showed a significant gradient between the second half of the 2000s and 2020 (Gil-Merino et al. 2018; Cornachione et al. 2020; Fian et al. 2021). We also note that the quasar activity was particularly high during this last period (see Gil-Merino et al. 2018, fig. 5).

The microlensing-induced variability of $F_{\rm opt}$ can be used, among other things, to constrain the size of concentric circular sources within the quasar accretion disc, where the observed optical continuum is mainly generated (e.g. Wambsganss 1998). Thus, considering Gaussian intensity profiles to model optical continuum sources, Fian et al. (2021) focused on a microlensing analysis of accurate *r*-band light curves of Q0957+561 over the period 1996−2016, and Cornachione et al. (2020) analysed a richer optical data set including additional *r*-band fluxes in the period 2008−2020 and *g*-band light curves from 2005 to 2020. The two independent studies led to similar values for the half-light radius of the *r*-band source, i.e. around 17.6 light-day and accurate to within a factor of ∼2−4 (see also Hainline et al. 2012; Jiménez-Vicente et al. 2014). Additionally, the microlensing-based size measurement of the *r*-band source is marginally consistent with a reverberation mapping analysis of Q0957+561 (Gil-Merino et al. 2012). Assuming that lags between optical bands correspond to light-travel times between flux-weighted mean radii of their sources (e.g. Fausnaugh et al. 2016), the reverberation-based half-light radius of the *r*-band source is only about 5 light-day, slightly above the lower limit of the 1σ interval reported by Cornachione et al. (2020). Interestingly, half-light radius increases with wavelength as predicted by the standard accretion disc (Gil-Merino et al. 2012).

If the contribution of diffuse light from BELR clouds to the optical continuum is significant (e.g. Korista & Goad 2001), the presence of extended sources should be taken into account when measuring accretion-disc source sizes from $F_{\rm opt}$ data. In fact, both diffuse continuum emission and broad-line emission contribute to some extent to optical passband fluxes (e.g. Sluse & Tewes 2014), and this contribution could be particularly important in Q0957+561 (e.g. Gil-Merino et al. 2018; Belete et al. 2019; Fian et al. 2021). In a scenario in which the BELR produces appreciable contamination in a given passband, the extinction-microlensing combined phenomenon would affect the extended and the nuclear (within the accretion disc) source differently. This should result in a non-standard flux ratio variability that would not be exclusively due to fluctuations in the microlens magnification ratio of the nuclear source. Interpreting observed flux ratio variations of Q0957+561 in different optical bands is thus a key task to understand the impact of BELR emissions on its multiband brightness.

The paper is organized as follows: In Section 2, we present multiband light curves of Q0957+561 spanning 44 yr, placing special emphasis on our accurate brightness records from frames taken at Teide and Roque de los Muchachos Observatories (Canary Islands) during the last 25 yr. In Section 3, we analyse the variability of the delay-corrected flux ratio in the *gVrR* bands. In Section 4, we try to link the observational results to BELR emissions. Relevant equations are incorporated into Appendix A, and a spectral analysis is presented in Appendix B.

2 OPTICAL LIGHT CURVES OF Q0957+561

Our optical monitoring of Q0957+561 started in 1996 using a CCD camera on the IAC80 telescope at Teide Observatory. Early frames for the period 1996−2001 were processed using the PHO2COM photometric task, which combines aperture photometry and PSF fitting (Serra-Ricart et al. 1999; Oscoz et al. 2002). Additionally, Gil-Merino et al. (2018) used the IMFITFITS software (McLeod et al. 1998) to process the most recent IAC80 *R*-band frames taken between 1999 January and 2005 November, and combined the *R*-band fluxes from IMFITFITS with those from PHO2COM in the period 1996−1998. The IMFITFITS software allows users to obtain an empirical PSF from the brightness profile of a field star, and then model the lens system as two stellar-like sources (quasar images A and B) plus a de Vaucouleurs profile convolved with the empirical PSF (main lens galaxy). In this paper, we also apply the IMFITFITS code to IAC80 *V*-band frames from early 1999 to 2005 November, and merge the new *V*-band data and the old *V*-band light curves in 1996−1998 (see above). Observations with the IAC80 telescope were carried out in a homogeneous way, using the same CCD camera and filters throughout the 10-yr campaign.

In addition to the IAC80 observations in the *V* and *R* bands, we considered frames in these optical bands that were taken with the Nordic Optical Telescope (NOT) in 2000 February–March (Ullán et al. 2003) and the AZT-22 telescope at Maidanak Astronomical Observatory (MT) in the period 2003−2005. These supplementary observations were processed using the IMFITFITS task. The NOT frames (and the IAC80 observations during 1999−2005) are available at the GLENDAMA data base,[1] whereas the MT frames were downloaded from the Lens Image Archive at the German Astrophysical Virtual Observatory.[2] Most IAC80–NOT–MT *V*-band magnitudes have not been published previously, and the total brightness records in the *V* band include data at 455 epochs (see the top panel of Fig. 1 and Table 1). The IAC80–NOT–MT *R*-band light curves contain magnitudes at 660 epochs (89 more epochs than those in Gil-Merino et al. 2018), and are shown in the bottom panel of Fig. 1 and Table 2.

Our ongoing monitoring in *gr* optical bands with the Liverpool Telescope (LT) at Roque de los Muchachos Observatory started soon after the first robotic science operations with this 2-m class telescope (Steele et al. 2004), and currently cover the period from 2005 January to 2023 June. The *gr* light curves of Q0957+561 over the first two decades of this century are based on the IMFITFITS task and have been described in some previous papers (Shalyapin et al. 2008; Shalyapin, Goicoechea & Gil-Merino 2012; Gil-Merino et al. 2018; Cornachione et al. 2020). Here, we add 3.5 yr of time coverage to the previous brightness records. The full data base incorporates *g*-band and *r*-band magnitudes at 621 and 639 epochs, respectively. For the entire 18.5-yr monitoring campaign with the LT, it is also worth noting that the median full width at half-maximum (FWHM) seeing was 1.60 arcsec, i.e. about four times smaller than the separation between quasar images. Additionally, the LT *r*-band light curves were combined with the United States Naval Observatory (USNO) data in the *r* band from 2007 December until 2017 April (105 epochs; see Hainline et al. 2012; Cornachione et al. 2020). The LT *g*-band light curves are depicted in the top panel of Fig. 2 and Table 3. The LT–USNO *r*-band light curves are shown in the bottom panel of Fig. 2 and Table 4.

Rudy Schild also compiled *R*-band data covering the first two decades after the discovery (1979−1998) and including magnitudes at 1233 epochs.[3] Hence, in order to construct historical records, we merged three data sets in red passbands: Rudy Schild's data base

[1] https://grupos.unican.es/glendama/database
[2] https://dc.zah.uni-heidelberg.de/lensunion/q/im/form
[3] https://lweb.cfa.harvard.edu/~rschild/

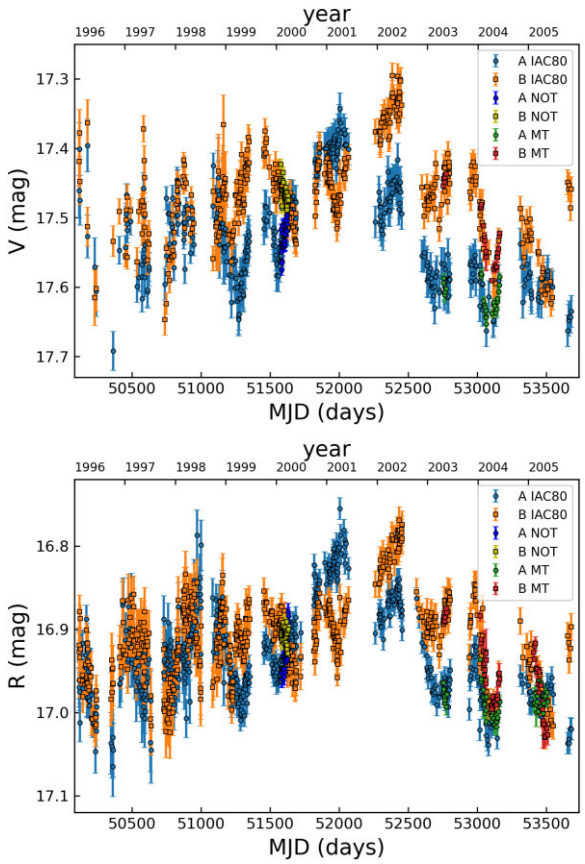

Figure 1. Optical light curves of Q0957+561. *Top*: IAC80–NOT–MT *V* band. *Bottom*: IAC80–NOT–MT *R* band.

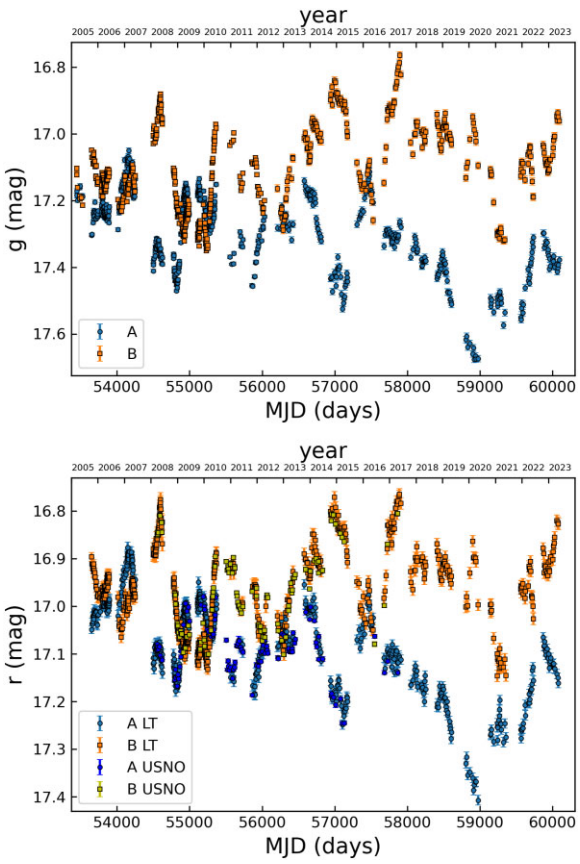

Figure 2. Optical light curves of Q0957+561. *Top*: LT *g* band. *Bottom*: LT–USNO *r* band.

Table 1. IAC80–NOT–MT *V*-band light curves of Q0957+561. The full table is available online in a machine-readable ASCII format. A portion is shown here for guidance regarding its form and content.

MJD	m_A (mag)	$\sigma(m_A)$ (mag)	m_B (mag)	$\sigma(m_B)$ (mag)	Tel
51586.051	17.543	0.013	17.466	0.010	IAC80
51586.830	17.565	0.008	17.483	0.008	NOT
51587.828	17.539	0.008	17.466	0.008	NOT
51589.071	17.541	0.023	17.461	0.018	IAC80
51591.022	17.526	0.023	17.449	0.018	IAC80

Table 2. IAC80–NOT–MT *R*-band light curves of Q0957+561. The full table is available online in a machine-readable ASCII format. A portion is shown here for guidance regarding its form and content.

MJD	m_A (mag)	$\sigma(m_A)$ (mag)	m_B (mag)	$\sigma(m_B)$ (mag)	Tel
52725.940	16.982	0.013	16.931	0.016	IAC80
52739.934	16.964	0.013	16.908	0.016	IAC80
52754.669	16.964	0.007	16.889	0.005	MT
52754.892	16.977	0.013	16.894	0.016	IAC80
52756.678	16.974	0.004	16.892	0.005	MT

Table 3. LT *g*-band light curves of Q0957+561. The full table is available online in a machine-readable ASCII format. A portion is shown here for guidance regarding its form and content.

MJD	m_A (mag)	$\sigma(m_A)$ (mag)	m_B (mag)	$\sigma(m_B)$ (mag)
53443.912	17.171	0.007	17.104	0.008
53445.893	17.184	0.007	17.122	0.008
53457.931	17.199	0.007	17.161	0.007
53486.876	17.161	0.007	17.187	0.007
53488.876	17.156	0.007	17.195	0.007

Table 4. LT–USNO *r*-band light curves of Q0957+561. The full table is available online in a machine-readable ASCII format. A portion is shown here for guidance regarding its form and content.

MJD	m_A (mag)	$\sigma(m_A)$ (mag)	m_B (mag)	$\sigma(m_B)$ (mag)
60028.015	17.130	0.010	16.867	0.012
60032.856	17.131	0.010	16.855	0.012
60060.869	17.142	0.010	16.820	0.012
60075.882	17.150	0.010	16.824	0.012
60081.909	17.161	0.010	16.827	0.012

in the *R* band, IAC80–NOT–MT *R* band, and LT–USNO *r* band. The historical records rely on magnitude offsets calculated from data in overlapping time segments between two different data sets, and they substantially extend the time coverage of Q0957+561 in red passbands (see Fig. 3). We have to remark that the oldest data show high measurement noise, while all data in the last 25 yr were obtained from state-of-the-art instruments and the same accurate photometric task, which significantly reduced noise.

3 FLUX RATIO IN THE *g V r R* BANDS

We initially selected the LT *g*-band light curves (see the top panel of Fig. 2 and Table 3) as a basic tool to understand properties of the variability of Q0957+561. The reasons for this choice are the homogeneity (only one telescope was used) and accuracy (all photometric errors are $\leq$1 per cent) of the data set, as well as its activity level (presence of the most conspicuous flux variations). In order to compare magnitudes of A and B at the same emission times, one has to account for the time delay between the two images. We assumed a concordance value $\Delta t = 420$ d (Kundić et al. 1997; Oscoz et al. 2001), and compared the light curve of B, $m_{\rm B}(t)$, and the time-shifted light curve of A, $m_{\rm A}(t - \Delta t)$ (see the top panel of Fig. 4). Both records were then fitted to linear laws describing long time-scale variabilities, and the best fits (dashed lines) were subtracted from the data. The resulting short time-scale variabilities $\Delta m_{\rm B}$ and $\Delta m_{\rm A}$ are depicted in the middle top panel of Fig. 4. There is a clear similitude between the short time-scale fluctuations in A and B, indicating that they are mainly due to quasar intrinsic variability.

To analyse the extrinsically induced differential variability, we have built the difference light curve (DLC) in the *g* band (see the middle bottom panel of Fig. 4). The DLC is the optical-passband flux ratio in terms of magnitudes, i.e. $m_{\rm B}(t) - m_{\rm A}(t - \Delta t) = -2.5\log(F_{\rm opt})$. The *g*-band differences $m_{\rm B}(t) - m_{\rm A}(t - \Delta t)$ are obtained using bins with 10-d semiwidth around the dates in B. Specifically, time-shifted magnitudes of A (and their uncertainties) are averaged within each non-empty bin that includes A data. As commented in Section 1, the DLC variability is exlusively caused by extrinsic effects. Thus, the *g*-band data lead to a long time-scale microlensing gradient in the DLC, which was modelled by a linear function. The best fit (dashed line) was then subtracted from the DLC. As can be seen in the bottom panel of Fig. 4, the resulting short time-scale residual signal $\Delta{\rm DLC} \equiv \Delta m_{\rm AB}$ is highly correlated with both $\Delta m_{\rm B}$ and $\Delta m_{\rm A}$, and therefore with the short time-scale intrinsic variability. This amazing result for a lensed quasar was previously anticipated (e.g. Sluse & Tewes 2014), and now inambiguously detected in Q0957+561.

At first glance, it seems a bit strange the existence of a correlation between intrinsic effects in the distant source and extrinsic effects in the main lens galaxy. Here, we look at it carefully considering all available data, whereas a plausible physical scenario to explain this correlation is discussed in Section 4. We have built a DLC in each optical passband and plotted the four difference signals in Fig. 5. We detect a clear gradual increase in the last 17 yr, although the positive gradient of the *r*-band DLC is slightly less pronounced than that in the *g* band. In addition, the *VR* difference curves are substantially noisier than the *gr* ones. The *VR* data are consistent with a flat signal around the year 2000, but the *V*-band DLC is also consistent with a smooth negative gradient in the period 1997−2005, which must be taken with caution. These three long time-scale gradients in the *gVr* bands were modelled by a linear function, while the *R*-band DLC has a more complex shape (it has a noticeable curvature around year 1990) and was fitted to a cubic function. The four best fits (dashed lines in Fig. 5) were subtracted from the corresponding DLCs, and the resulting residual signals were then used to construct $\Delta m_{\rm AB}$–$\Delta m_{\rm B}$ diagrams (see Fig. 6). We note that the short time-scale variability of B, $\Delta m_{\rm B}$, is a good proxy for the short time-scale intrinsic variability (see above).

The four diagrams in Fig. 6 reveal the correlation between extrinsically induced differential variations on short time-scales and intrinsic variations on those time-scales. To check the significance of this correlation in each band, we performed a linear regression analysis assuming the relationship $\Delta m_{\rm AB} = \gamma \Delta m_{\rm B}$. The results are shown in Table 5. There is a weak correlation in the *VR* bands (PCC $\sim$ 0.2−0.3), but it is strong in the *gr* bands (PCC $\sim$ 0.8). These numerical results agree well with a visual inspection of Fig. 6. Additionally, Table 5 includes the reduced chi-square values for the linear/cubic fits to the DLCs (dashed lines in Fig. 5). The last column also shows the chi-square values for linear/cubic fits to corrected DLCs, i.e. when $\gamma \Delta m_{\rm B}$ contributions are subtracted from each difference signal. The improvement in the *gr* bands is notable, while $\chi^2_{\rm DLC*} \sim \chi^2_{\rm DLC}$ in the *VR* bands. From the values of PCC and $\Delta\chi^2 = \chi^2_{\rm DLC} - \chi^2_{\rm DLC*}$, we conclude that accuracy and activity level play a role in detecting the elusive correlation that we are discussing.

Turning our attention once more to the data in the *g* and *r* bands, we have also carried out a simultaneous fit of four free parameters in each optical band: time delay (Δt), intercept (a) and slope (b) of the linear fit to the DLC, and slope (γ) of the linear regression on $\Delta m_{\rm AB}$ with $\Delta m_{\rm B}$. In order to fit these parameters, we minimized the dispersion between $m_{\rm B}(t)$ and the four-parametric model $m_{\rm Bm}(t) = m_{\rm A}(t - \Delta t) + a + bt + \gamma \Delta m_{\rm B}(t)$ (the minimum dispersion technique is discussed in Pelt et al. 1996, and references therein). Using 1000 bootstrap samples and a decorrelation length of 15 d, Fig. 7 shows all best-fit solutions in the two-dimensional (γ, Δt) space. This Fig. 7 also displays 1σ (along with 2σ and 3σ) intervals in each passband, i.e. $\gamma = 0.201 \pm 0.004$ and $\Delta t = 420.22 \pm 0.60$ d in the *g* band, and $\gamma = 0.227 \pm 0.007$ and $\Delta t = 418.85 \pm 0.66$ d in the *r* band. In Fig. 8, we also compared the *g*-band light curve of B and two different models of that curve, i.e. a standard model exclusively incorporating a microlensing gradient, $m_{\rm Bm0}(t) = m_{\rm A}(t - \Delta t) + a + bt$, and the four-parametric model emerging from our analysis, $m_{\rm Bm}(t)$. It is clear that the refined model works better than the standard one.

4 DISCUSSION

The first lensed quasar has two optically bright and widely separated images whose brightness has been monitored since 1979 for thousands of nights. Therefore, its light curves offer a unique opportunity to probe the possible existence of nuclear and extended sources (e.g. Barkana 1997), or unnoticed details of the accretion disc (e.g. Blackburne & Kochanek 2010). Sluse & Tewes (2014) highlighted the important contribution of BELR emissions to optical passband fluxes, and the BELR radiation appears to play a role in Q0957+561 (Gil-Merino et al. 2018; Belete et al. 2019) and other lens systems (Paic et al. 2022; Fian, Chelouche & Kaspi 2023a). Thus, to try to account for the observed correlation between extrinsic and intrinsic short time-scale variations of Q0957+561 in the *gr* bands (see Section 3), we decided to focus on BELR radiation contaminating the nuclear emission from the accretion disc (see Appendix A). This includes a diffuse continuum and blended weak iron lines, with some contribution from a broad-line (C III] or Mg II; see Appendix B). Although a small fraction of line emissions may arise from relatively compact regions (e.g. Fian et al. 2018, 2023b), we also considered that the BELR is large enough to ignore microlensing effects.

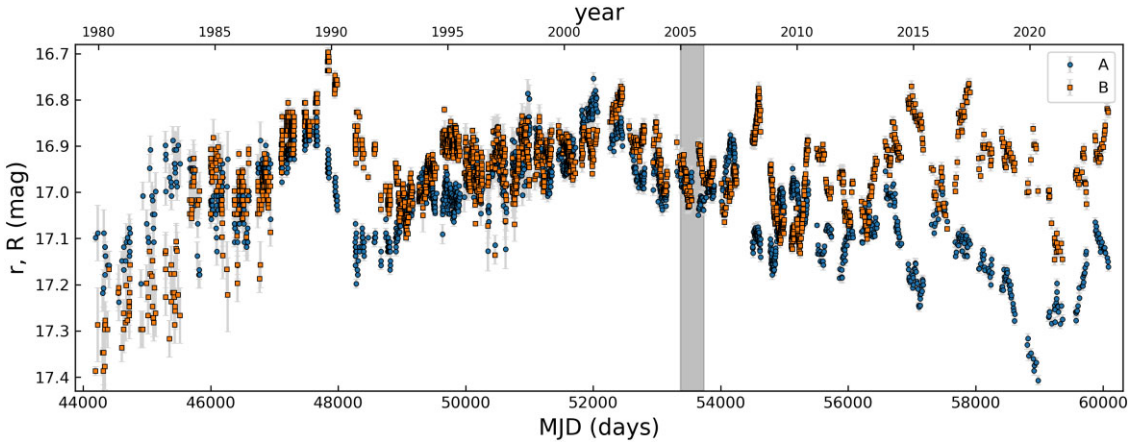

Figure 3. Historical brightness records in red passbands from 1979 to 2023. The shaded bar highlights the time segment in which the IAC80–NOT–MT *R*-band and LT–USNO *r*-band data sets overlap (see main text).

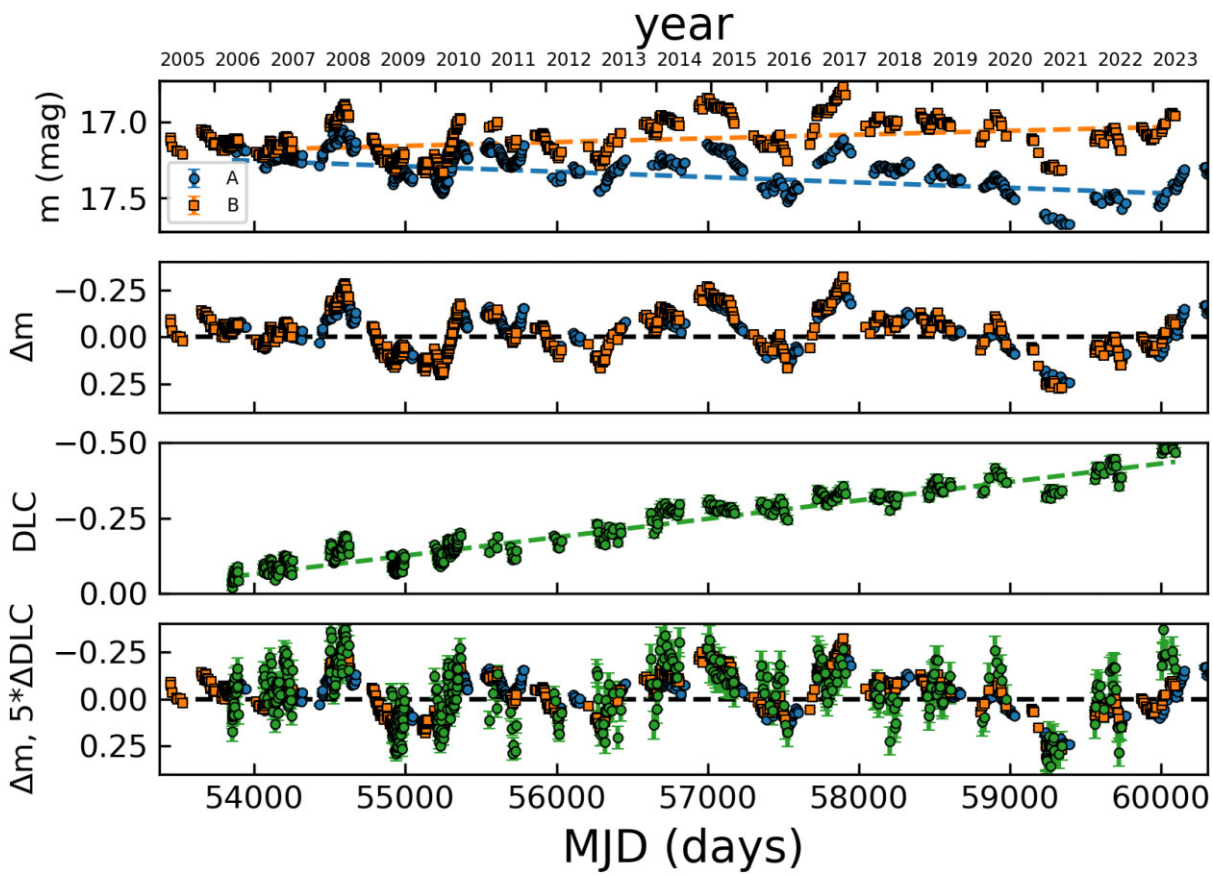

Figure 4. AB comparison in the *g* band. *Top*: Light curves of A and B. We use original data of B and magnitudes of A shifted by 420 d (see main text). Best linear fits to data are also shown (dashed lines). *Middle top*: Residual signals of A and B after subtracting linear trends. *Middle bottom*: DLC and the best linear fit to it (dashed line). The DLC is constructed using bins with 10-d semiwidth around the dates in B. *Bottom*: All residual signals after subtracting linear trends. The DLC residuals ΔDLC are multiplied by a factor 5 to improve their visibility.

To properly interpret the measured slope of the linear regression on $\Delta m_{\rm AB}$ with $\Delta m_{\rm B}$, we must take into account equation (A12), and estimate dust extinctions and microlensing magnifications. According to previous ideas about this double quasar, its BELR is not suffering appreciable extinction effects, since the C III] and Mg II flux ratios are consistent with the flux ratio from radio data (e.g. Schild & Smith 1991; Garrett et al. 1994; Gil-Merino et al. 2018). This translates to $\epsilon^*_{\rm A} \approx \epsilon^*_{\rm B} \approx 1$. During a quiescent phase of microlensing activity around the year 2000 (see Section 3), *HST* spectra of Q0957+561 have also made it possible to measure the 'continuum'

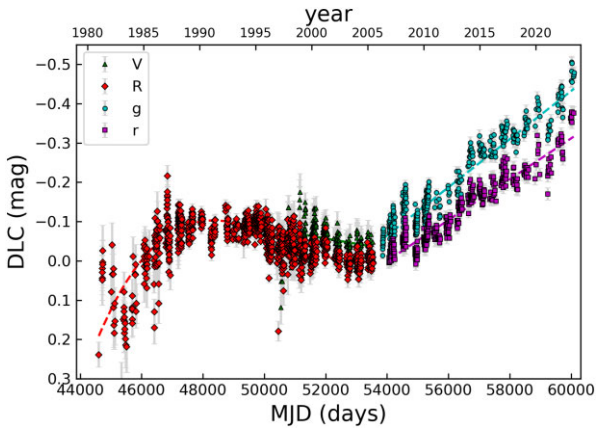

Figure 5. Difference light curves in the *gVrR* bands. Best fits to shapes on long time-scales (dashed lines) rely on a linear function (*gVr* bands) and a cubic law (*R* band).

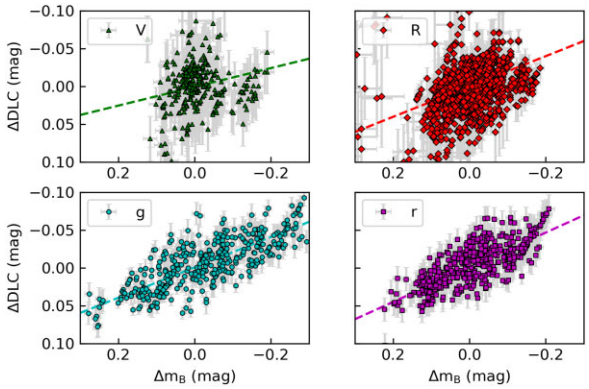

Figure 6. $\Delta m_{\rm AB}$–$\Delta m_{\rm B}$ diagrams. Dashed lines represent linear regression fits going through the origin.

Table 5. Linear regression on $\Delta m_{\rm AB}$ with $\Delta m_{\rm B}$. Columns 2–7 list the number of observing epochs in the light curves, the number of AB pairs when A is shifted by 420 d, the reduced chi-square value for the linear/cubic fit to the DLC (see Fig. 5), the slope of the linear regression (see Fig. 6), the Pearson correlation coefficient (PCC), and the reduced chi-square value for a linear/cubic fit to a corrected DLC: $\mathrm{DLC}_* = \mathrm{DLC} - \gamma\,\Delta m_{\rm B}$, respectively.

Band	$N_{\rm obs}$	$N_{\rm AB}$	$\chi^2_{\rm DLC}$	γ	PCC	$\chi^2_{\rm DLC*}$
V	455	323	1.192	0.119	0.204	1.160
R	1893	1431	1.812	0.204	0.324	1.812
g	621	402	3.144	0.201	0.773	1.991
r	744	491	1.929	0.228	0.756	1.303

flux ratio at several UV–optical wavelengths.[4] These measurements were consistent with the absence of microlensing effects and the presence of a significant dust extinction in the main lens galaxy (Goicoechea et al. 2005). Adopting a (macro)lens magnification ratio $M_{\rm B}/M_{\rm A} = 0.75$ from radio-core data and assuming that dust is mainly affecting the nuclear continuum in the A image ($\epsilon_{\rm B} \approx 1$), the *HST* data provided the constraints $\epsilon_{\rm A}(g) \approx \epsilon_{\rm A}(r) \approx 0.7(1+\eta) - \eta$ in the *gr* bands.

[4] 'Continuum' refers to the nuclear continuum plus the diffuse continuum and pseudo-continuum from the BELR.

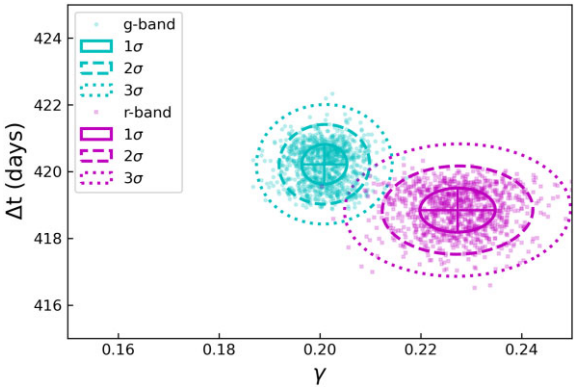

Figure 7. Best-fit solutions in the two-dimensional parameter space (γ, Δt). These solutions rely on 1000 bootstrap samples and the minimum dispersion technique with 15-d decorrelation length (see main text).

Regarding microlensing magnifications of the nuclear continuum, the microlensing linear gradients of the DLCs in the *gr* bands (see Fig. 5) are most likely generated within the high-density region of the main lens galaxy that is crossed by image B, i.e. $\mu_{\rm B} \gtrsim 1$ and $\mu_{\rm A} \approx 1$. Refsdal et al. (2000) also considered microlensing effects on this image to interpret the early fluctuation of the DLC in the *R* band. From the observed linear gradients in the *gr* bands and the $\epsilon_{\rm A} - \eta$ relationship in the previous paragraph, we obtained additional constraints on the time-averaged microlensing magnifications of the nuclear continuum in B: $\overline{\mu_{\rm B}}(g) \approx 1.2(1+\eta) - \eta$ and $\overline{\mu_{\rm B}}(r) \approx 1.1(1+\eta) - \eta$. We have then reproduced the γ values in Table 5 by using equation (A12) and all extinction-magnification constraints, as well as $\eta \approx 0.25$ and $\eta \approx 0.3$ for the *g* and *r* bands, respectively. These η values roughly coincide with fiducial ones (e.g. Sluse & Tewes 2014; Fian et al. 2023a), supporting and encouraging more detailed studies of BELR emissions in Q0957+561. It is also important to emphasize that the tension between the microlensing-based size of the *r*-band source and its reverberation-based value may be due to an overestimation of the size from microlensing studies, which did not consider the contribution of the BELR (e.g. see fig. 4 of Fian et al. 2023a).

Equations (A3) and (A4) allow us to estimate diffuse-to-total flux ratios in the *gr* bands. The relative contributions of diffuse light are thus ∼28–29 per cent (A) and ∼17 per cent (B) in the *g* band, and ∼33 per cent (A) and ∼21 per cent (B) in the *r* band. The diffuse light from the BELR includes emission lines and continuum emission (scattered and thermal radiation), so an analysis of optical spectra of Q0957+561 in the wavelength ranges covered by the *g* and *r* bands should shed light on the nature of the dominant diffuse component in these two Sloan passbands. Accordingly to the diffuse-to-total flux ratios and the final results of the spectral analysis in Appendix B, the diffuse continuum component accounts for about 24 per cent of the total flux of A and ∼13–14 per cent of the total flux of B. This means that the diffuse continuum component is 3.5–5 times greater than the lines component in the *g* band, whereas it is 2–3 times greater than the lines component in the *r* band. The diffuse-to-nuclear continuum emission ratio is $\eta_{\rm cont} \approx 0.2$ in both optical bands, and detailed polarimetric observations could help to unveil the origin of the non-nuclear continuum (e.g. Hutsemékers et al. 2015; Hutsemékers, Sluse & Kumar 2020; Popović et al. 2021).

Finally, in the two passbands, the diffuse continuum emission is greater than the lines emission, i.e. diff. continuum/lines $= (\eta/\eta_{\rm cont} - 1)^{-1} \sim 3$. The diff. continuum/lines ratio depends on the BELR

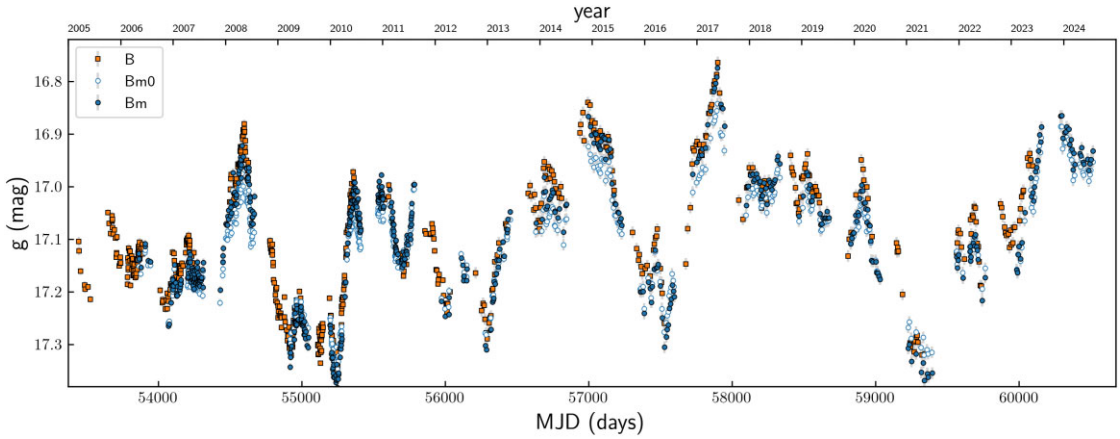

Figure 8. The *g*-band light curve of the image B and two models for it. The observed magnitudes (B) are compared with magnitudes predicted by a standard model (Bm0) and those predicted by a refined model (Bm; see main text for details).

geometry and physics, and the development of a detailed realistic model for Q0957+561 is a pending task that is out of the scope of this paper.

ACKNOWLEDGEMENTS

We thank Carina Fian for insightful comments on diffuse emission in quasars and Rudy Schild for making publicly available brightness records of Q0957+561 from 1979 to 1998. We are grateful to Evencio Mediavilla, Miquel Serra-Ricart, Rodrigo Gil-Merino, and Aurora Ullán, among others, for their critical participation in several phases of the project to accurately follow-up the activity of Q0957+561 from facilities located in the Canary Islands. We also thank the anonymous referee for helpful comments that contributed to improve the original manuscript. This paper is mainly based on observations made with the IAC80 telescope and the Liverpool Telescope (LT). The IAC80 telescope is operated on the island of Tenerife by the Instituto de Astrofísica de Canarias (IAC) in the Spanish Observatorio del Teide. The LT is operated on the island of La Palma by Liverpool John Moores University in the Spanish Observatorio del Roque de los Muchachos of the IAC with financial support from the UK Science and Technology Facilities Council. We also use frames taken with the Nordic Optical Telescope and the AZT-22 telescope at Maidanak Observatory (MT), thank the staff of all telescopes for a kind interaction, and are grateful to the institutions developing and funding the German Astrophysical Virtual Observatory where the MT data are stored. VNS would like to thank the Universidad de Cantabria (UC) and the Spanish Agencia Estatal de Investigacion (AEI) for financial support for a long stay at the UC in the period 2022–2024. This research has been supported by the grant PID2020-118990GB-I00 funded by MCIN/AEI/10.13039/501100011033.

DATA AVAILABILITY

The paper mainly relies on light curves in the *gVrR* bands in the period 1996–2023 that are shown in Tables 1 (*V* band), 2 (*R* band), 3 (*g* band), and 4 (*r* band). These light curves correspond to observations with several telescopes, and most optical frames taken since 1999 are available at different repositories: GLENDAMA Database (https://grupos.unican.es/glendama/database; IAC80 telescope, Nordic Optical Telescope, and observations with the Liverpool Telescope until 2016), Lens Image Archive of the German Astrophysical Virtual Observatory (https://dc.zah.uni-heidelberg.de/lensunion/q/im/form; AZT-22 telescope at Maidanak Astronomical Observatory), and LT Data Archive (https://telescope.livjm.ac.uk/cgi-bin/lt_search; Liverpool Telescope). Additional *R*-band photometric data from 1979 to 1998 were collected by Rudy Schild and are available at https://lweb.cfa.harvard.edu/~rschild/. The spectral analysis in Appendix B relies on observations available at the LT Data Archive and spectra at https://cdsarc.u-strasbg.fr/viz-bin/qcat?J/A + A/616/A118.

REFERENCES

Barkana R., 1997, ApJ, 489, 21
Belete A. B., Canto Martins B. L., Leão I. C., De Medeiros J. R., 2019, MNRAS, 484, 3552
Blackburne J. A., Kochanek C. S., 2010, ApJ, 718, 1079
Chang K., Refsdal S., 1979, Nature, 282, 561
Conner S. R., Lehar J., Burke B. F., 1992, ApJ, 387, L61
Cornachione M. A., Morgan C. W., Burger H. R., Shalyapin V. N., Goicoechea L. J. , Vrba F. J., Dahm S. E. , Tilleman T. M., 2020, ApJ, 905, A7
Fausnaugh M. M. et al., 2016, ApJ, 821, A56
Fian C., Guerras E., Mediavilla E., Jiménez-Vicente J., Muñoz J. A., Falco E. E., Motta V., Hanslmeier A., 2018, ApJ, 859, A50
Fian C. et al., 2021, A&A, 654, A70
Fian C., Chelouche D., Kaspi S., 2023a, A&A, 677, A94
Fian C. et al., 2023b, A&A, 678, A108
Garrett M. A., Walsh D., Carswell R. F., 1992, MNRAS, 254, 27P
Garrett M. A., Calder R. J., Porcas R. W., King L. J. , Walsh D., Wilkinson P. N., 1994, MNRAS, 270, 457
Gil-Merino R., Goicoechea L. J., Serra-Ricart M., Oscoz A., Alcalde D., Mediavilla E., 2001, MNRAS, 322, 397
Gil-Merino R., Goicoechea L. J., Shalyapin V. N., Braga V. F., 2012, ApJ, 744, A47
Gil-Merino R., Goicoechea L. J., Shalyapin V. N., Oscoz A., 2018, A&A, 616, A118
Goicoechea L. J., Gil-Merino R., Ullán A., 2005, MNRAS, 360, L60
Hainline L. J. et al., 2012, ApJ, 744, A104
Hutsemékers D., Sluse D., Braibant L., Anguita T., 2015, A&A, 584, A61
Hutsemékers D., Sluse D., Kumar P., 2020, A&A, 633, A101
Jiménez-Vicente J., Mediavilla E., Kochanek C. S., Muñoz J. A., Motta V., Falco E., Mosquera A. M., 2014, ApJ, 783, A47
Korista K. T., Goad M. R., 2001, ApJ, 553, 695
Kundić T. et al., 1997, ApJ, 482, 75
Kuraszkiewicz J. K., Green P. J., Forster K., Aldcroft T. L., Evans I. N., Koratkar A., 2002, ApJS, 143, 257
Maoz D. et al., 1993, ApJ, 404, 576
McLeod B. A., Bernstein G. M., Rieke M. J., Weedman D. W., 1998, ApJ, 115, 1377

Nadeau D., Yee H. K. C., Forrest W. J., Garnett J. D. , Ninkov Z. , Pipher J. L., 1991, ApJ, 376, 430
Oscoz A., Mediavilla E., Goicoechea L. J., Serra-Ricart M., Buitrago J., 1997, ApJ, 479, L89
Oscoz A. et al., 2001, ApJ, 552, 81
Oscoz A., Alcalde D., Serra-Ricart M., Mediavilla E., Muñoz J. A., 2002, ApJ, 573, L1
Paic E., Vernardos G., Sluse D., Millon M., Courbin F., Chan J. H., Bonvin V., 2022, A&A, 659, A21
Pelt J., Kayser R., Refsdal S., Schramm T., 1996, A&A, 305, 97
Popović, L. Č., Afanasiev V. L., Shablovinskaya E. S., Ardilanov V. I., Savić, Dj., 2021, A&A, 647, A98
Refsdal S., Stabell R., Pelt J., Schild R., 2000, A&A, 360, 10
Schild R. E., Smith R. C., 1991, AJ, 101, 813
Serra-Ricart M., Oscoz A., Sanchís T., Mediavilla E., Goicoechea L. J., Licandro J., Alcalde D., Rodrigo G-M., 1999, ApJ, 526, 40
Shakura N. I., Sunyaev R. A., 1973, A&A, 24, 337
Shalyapin V. N., Goicoechea L. J., Koptelova E., Ullán A., Gil-Merino R., 2008, A&A, 492, 401
Shalyapin V. N., Goicoechea L. J., Gil-Merino R., 2012, A&A, 540, A132
Sluse D., Tewes M., 2014, A&A, 571, A60
Steele I. A. et al., 2004, Proc. SPIE, 5489, 679
Stockton A., 1980, ApJ, 242, L141
Tsuzuki Y., Kawara K., Yoshii Y., Oyabu S., Tanabé T., Matsuoka Y., 2006, ApJ, 650, 57
Ullán A. et al., 2003, MNRAS, 346, 415
Vanderriest C., Schneider J., Herpe G., Chevreton M., Moles M., Wlerick G., 1989, A&A, 215, 1
Vestergaard M., Wilkes B. J., 2001, ApJS, 134, 1
Walsh D., Carswell R. F., Weymann R. J., 1979, Nature, 279, 381
Wambsganss J., 1998, Living Rev. Relativ., 1, 12
Wills B. J., Netzer H., Wills D., 1985, ApJ, 288, 94
Young P., Gunn J. E., Oke J. B., Westphal J. A., Kristian J., 1980, ApJ, 241, 507

SUPPORTING INFORMATION

Supplementary data are available at *MNRAS* online.

suppl_data

Please note: Oxford University Press is not responsible for the content or functionality of any supporting materials supplied by the authors. Any queries (other than missing material) should be directed to the corresponding author for the article.

APPENDIX A: ADDING BELR PHOTONS TO THE ACCRETION DISC RADIATION

It is thought that optical passband fluxes of quasars are mainly generated in tiny accretion discs around central supermassive black holes (e.g. Shakura & Sunyaev 1973). For a non-lensed quasar, the accretion-disc flux observed at time t in a given passband can be assumed to consist of two components: a slowly varying component $f_0(t)$ and a small contribution that varies more rapidly $\varphi(t)$. Thus,

$$f_{\rm disc}(t) = f_0(t) + \varphi(t) = f_0(t)[\,1 + \delta(t)]\,, \tag{A1}$$

with $\delta(t) = \varphi(t)/f_0(t)$ and $|\delta| << 1$.

In a given passband, in addition to the nuclear continuum emission (thermal radiation from the accretion disc), it is expected to detect a diffuse continuum emission (scattered and thermal radiation from the BELR; e.g. Korista & Goad 2001), a pseudo-continuum emission (heavily blended weak iron lines produced in the BELR; e.g. Wills, Netzer & Wills 1985; Maoz et al. 1993), and some contribution from a broad-line within the spectral coverage of the passband. In brief, accretion-disc photons would be mixed with photons coming from the BELR. If T is the average light-travel time (in the observer frame) between the nuclear source and the BELR clouds, and $\eta << 1$ is the BELR-to-nuclear emission ratio, then

$$f_{\rm BELR}(t) = \eta[\,f_0(t-T) + \varphi_{\Delta T}(t-T)] = \eta\, f_0(t-T)(1+\delta^*). \tag{A2}$$

Here, the rapidly varying component is smoothed out over a time-scale $\Delta T \sim 2T$ representing the light-crossing time of the BELR, and $\delta^* = \varphi_{\Delta T}(t-T)/f_0(t-T)$.

In the presence of a lensing galaxy, the observer sees two different images, A and B, of the background quasar. If we consider an individual image, e.g. B, in general, the flux $f_{\rm disc}$ in equation (A1) is affected by the macrolens magnification $M_{\rm B}$, a microlens magnification $\mu_{\rm B}$, and a dust extinction $\epsilon_{\rm B}$, and additionally, the corresponding photons arrive at the observer delayed by a time $\tau_{\rm B}$ with respect to their travel time in the absence of a gravitational deflector. Assuming that the extended (BELR) source is not suffering appreciable microlensing effects and renaming $t + \tau_{\rm B}$ as t, the flux of the B image is given by

$$\begin{aligned} F_{\rm B}(t) &= M_{\rm B}[\,\mu_{\rm B}\epsilon_{\rm B}\, f_0(t)(1+\delta) + \epsilon^*_{\rm B}\eta\, f_0(t-T)(1+\delta^*)] \\ &= M_{\rm B}\mu_{\rm B}\epsilon_{\rm B}\, f_0[\,1 + \delta + \alpha_{\rm B}(1+\delta^*)]\,, \end{aligned} \tag{A3}$$

where ϵ^* represents the dust extinction of the extended source and $\alpha = (\epsilon^*/\epsilon)(\eta/\mu)[f_0(t-T)/f_0(t)] \approx (\epsilon^*/\epsilon)(\eta/\mu)$, since the variability time-scale of f_0 is much longer than T. Although we have simplified notation in the final expression of $F_{\rm B}(t)$ in equation (A3), the parameters f_0, $\mu_{\rm B}$, δ, δ^*, and $\alpha_{\rm B}$ are functions of time. Taking into account the time delay Δt between A and B, the flux of A at the same emission time is

$$F_{\rm A}(t-\Delta t) = M_{\rm A}\mu_{\rm A}\epsilon_{\rm A}\, f_0[\,1 + \delta + \alpha_{\rm A}(1+\delta^*)]\,. \tag{A4}$$

From equations (A3) and (A4), the optical-passband flux ratio can be written as

$$F_{\rm opt} = F_{\rm B}(t)/F_{\rm A}(t-\Delta t) = \Phi_{\rm AB} C, \tag{A5}$$

where

$$\Phi_{\rm AB} = \frac{M_{\rm B}\mu_{\rm B}\epsilon_{\rm B}(1+\alpha_{\rm B})}{M_{\rm A}\mu_{\rm A}\epsilon_{\rm A}(1+\alpha_{\rm A})} \tag{A6}$$

and

$$C = \frac{1 + (\delta + \alpha_{\rm B}\delta^*)/(1+\alpha_{\rm B})}{1 + (\delta + \alpha_{\rm A}\delta^*)/(1+\alpha_{\rm A})}. \tag{A7}$$

Assuming that $|\delta|$, $|\delta^*|$, $|\alpha| << 1$, and expanding C up to second order: $C \approx 1 + (\delta - \delta^*)(\alpha_{\rm A} - \alpha_{\rm B})$, the flux ratio is approximated as

$$F_{\rm opt} \approx \Phi_{\rm AB}[\,1 + (\delta - \delta^*)(\alpha_{\rm A} - \alpha_{\rm B})]\,. \tag{A8}$$

Taking the logarithm on both sides of equation (A8), multiplying by -2.5, and assuming the presence of long time-scale microlensing events, the short time-scale residual signal is

$$\begin{aligned} \Delta m_{\rm AB} &= m_{\rm B}(t) - m_{\rm A}(t-\Delta t) - dm_{\rm AB} \\ &\approx -1.086(\delta - \delta^*)(\alpha_{\rm A} - \alpha_{\rm B}), \end{aligned} \tag{A9}$$

with $dm_{\rm AB} = -2.5\log \Phi_{\rm AB}$. This residual signal is related to the short time-scale intrinsic variability.

It is reasonable to assume that the rapidly varying component φ has larger amplitudes than its smoothed version in equation (A2), and neglecting the contribution of $\varphi_{\Delta T}$ (i.e. $\delta^* \approx 0$) to facilitate the discussion in Section 4,

$$\Delta m_{\rm AB} \approx -1.086\,\delta(\alpha_{\rm A} - \alpha_{\rm B}). \tag{A10}$$

The flux of the B image (see equation (A3) for $\delta^* \approx 0$) can be rewritten as $F_B = F_{B0}[\,1 + \delta/(1+\alpha_B)]$, where $F_{B0} = M_B \mu_B \epsilon_B (1+\alpha_B) f_0$. This leads to $F_B/F_{B0} \approx 1+\delta$, and $\delta = (f_{disc} - f_0)/f_0 \approx (F_B - F_{B0})/F_{B0} \approx -0.921(m_B - m_{B0}) = -0.921\Delta m_B$. The solution for the residues is then

$$\Delta m_{AB} \approx \Delta m_B(\alpha_A - \alpha_B). \tag{A11}$$

The residues Δm_{AB} are directly correlated with the magnitude fluctuations in both images (with respect to slow components m_{A0} and m_{B0}), and the parameter of interest is

$$\gamma \approx \alpha_A - \alpha_B \approx \eta \left(\frac{\epsilon_A^*}{\mu_A \epsilon_A} - \frac{\epsilon_B^*}{\mu_B \epsilon_B} \right). \tag{A12}$$

APPENDIX B: OPTICAL SPECTRA AND SLOAN PASSBANDS

We selected spectroscopic observations taken with the LT on 2015 November 19 (image A) and 2017 January 17 (image B) for further analysis. They are separated by the time delay of the system (same emission time), correspond to central dates in our LT monitoring campaign, and were presented in fig. 7 of Gil-Merino et al. (2018) (see also Fian et al. 2023b).The LT spectra covering the *g*-band transmission window are shown in Fig. B1. This Fig. B1 also includes simple data decompositions into three components (ignoring some minor emission lines and absorption features), which are enough for our purpose. Each decomposition (model) consists of a power-law continuum, an iron pseudo-continuum (iron forest), and a Gaussian component around the vertical dotted line (C III] emission). The power-law continuum was determined from data in two spectral windows that barely contain iron emission (shaded bars; e.g. Kuraszkiewicz et al. 2002), while we used the Vestergaard & Wilkes (2001) template to estimate the iron pseudo-continuum. To account for instrumental and Doppler broadenings, this template was convolved with a Gaussian function. The LT spectra covering the *r*-band transmission window are also shown in Fig. B2, where data decompositions into three components were made in a similar way to those in Fig. B1. The 'pure' continuum windows are shaded (e.g. Kuraszkiewicz et al. 2002), the Fe II pseudo-continuum of each quasar image is based on the Tsuzuki et al. (2006) template, and the Gaussian components around the vertical dotted lines represent the Mg II emission.

Using the response curve and models in Fig. B1, we obtained lines(Fe + C III])-to-total flux ratios of 4.7 per cent (A) and 3.8 per cent (B) in the *g* band. From the response curve and models in Fig. B2, the lines(Fe II + Mg II)-to-continuum flux ratios in the *r* band are about twice those in the *g* band, i.e. 8.7 per cent (A) and 6.6 per cent (B).

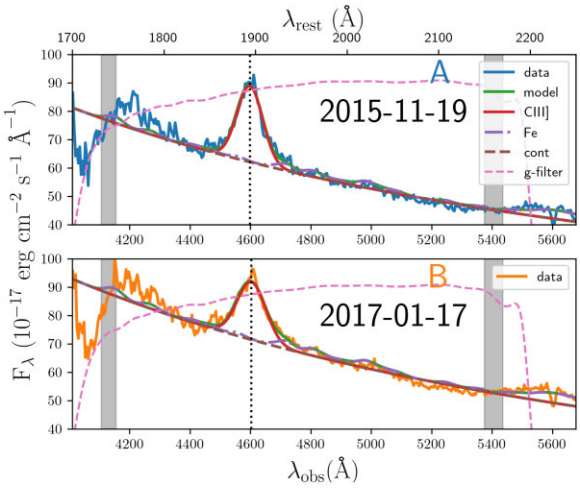

Figure B1. LT spectra of the two quasar images in the transmission window of the *g* band. Dashed lines describe the response curve of the LT *g*-Sloan filter. Each spectrum is roughly modelled as a sum of three contributions: power-law continuum, iron pseudo-continuum, and C III] emission line (see main text).

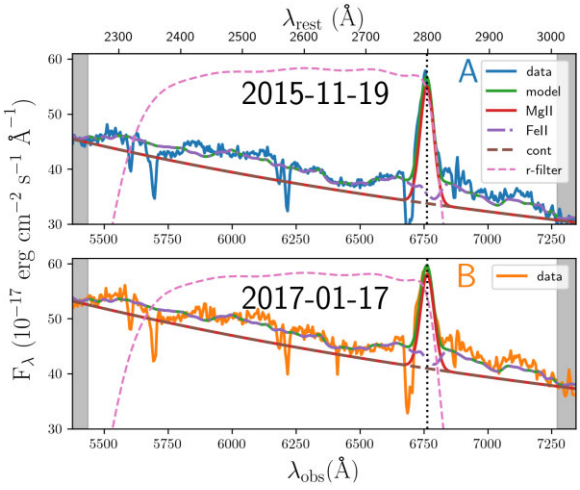

Figure B2. LT spectra of the two quasar images in the transmission window of the *r* band. Dashed lines describe the response curve of the LT *r*-Sloan filter. Each spectrum is roughly modelled as a sum of three contributions: power-law continuum, Fe II pseudo-continuum, and Mg II emission line (see main text).

This paper has been typeset from a TEX/LATEX file prepared by the author.